*J. Fluid Mech.* (2006), *vol.* 563, *pp.* 415–441. © 2006 Cambridge University Press
doi:10.1017/S0022112006001236 Printed in the United Kingdom

# Numerical simulation of lowest-order short-crested wave instabilities

By DAVID R. FUHRMAN, PER A. MADSEN AND HARRY B. BINGHAM

Department of Mechanical Engineering, Technical University of Denmark,
DK-2800 Kgs. Lyngby, Denmark

(Received 28 June 2005 and in revised form 21 February 2006)

A numerical study of doubly periodic deep-water short-crested wave instabilities, arising from various quartet resonant interactions, is conducted using a high-order Boussinesq-type model. The model is first verified through a series of simulations involving classical class I plane wave instabilities. These correctly lead to well-known (nearly symmetric) recurrence cycles below a previously established breaking threshold steepness, and to an asymmetric evolution (characterized by a permanent transfer of energy to the lower side-band) above this threshold, with dissipation from a smoothing filter promoting this behaviour in these cases. A series of class Ia short-crested wave instabilities, near the plane wave limit, are then considered, covering a wide range of incident wave steepness. A close match with theoretical growth rates is demonstrated near the inception. It is shown that the unstable evolution of these initially three-dimensional waves leads to an asymmetric evolution, even for weakly nonlinear cases presumably well below breaking. This is characterized by an energy transfer to the lower side-band, which is also accompanied by a similar transfer to more distant upper side-bands. At larger steepness, the evolution leads to a permanent downshift of both the mean and peak frequencies, driven in part by dissipation, effectively breaking the quasi-recurrence cycle. A single case involving a class Ib short-crested wave instability at relatively large steepness is also considered, which demonstrates a reasonably similar evolution. These simulations consider the simplest physical situations involving three-dimensional instabilities of genuinely three-dimensional progressive waves, revealing qualitative differences from classical two-dimensional descriptions. This study is therefore of fundamental importance in understanding the development of three-dimensional wave spectra.

## 1. Introduction

The nonlinear evolution of unstable surface wavetrains is of fundamental importance to the understanding of wave spectrum development. Up to now, most studies regarding the nonlinear evolution of the lowest-order class I (Benjamin & Feir 1967) instability have been two-dimensional. This is true of wave-tank experiments (e.g. Lake *et al.* 1977; Melville 1982; Tulin & Waseda 1999), analytical investigations (e.g. Stiassnie & Kroszynski 1982), as well as numerical simulations (e.g. Lo & Mei 1985; Madsen, Bingham & Liu 2002). This is justifiably the case, as the dominant class I instability is indeed two-dimensional, as shown, for example, in the analysis of McLean (1982*b*). It should be mentioned, however, that Lo & Mei (1987) and Trulsen & Dysthe (1997) have also simulated three-dimensional class I instabilities, in the latter case demonstrating a frequency downshift in the absence of dissipation (this finding is backed further by the experimental work of Trulsen, Stansberg & Velarde 1999). Shemer & Chamesse (1999) have additionally made numerical and experimental investigations of three-dimensional gravity–capillary wave instabilities. Numerous authors have also studied the predominantly three-dimensional class II plane wave instability in a weakly nonlinear (e.g. Stiassnie & Shemer 1987; Shrira, Badulin & Kharif 1996), as well as a fully-nonlinear context (Xue *et al.* 2001; Fuhrman, Madsen & Bingham 2004; Fructus *et al.* 2005), leading to spectacular crescent-shaped surface patterns (see also the experimental work of, e.g. Melville 1982; Su *et al.* 1982). However, this type of instability becomes dominant only when the incident wave steepness is relatively large.

As a result of these (and numerous other) studies, the dynamics of plane wave instabilities are by now relatively well, though by no means completely, understood. In contrast, relatively little attention has been paid to the unstable evolution of genuinely three-dimensional wavetrains, which are of interest, as strictly two-dimensional carrier waves are rare in the open sea. The simplest progressive three-dimensional wave patterns are so-called short-crested waves, defined here simply as doubly periodic wave patterns that are progressive in a single horizontal dimension. Steady solutions of various orders for such three-dimensional wave patterns have been provided, for example, by Hsu, Tsuchiya & Silvester (1979), Roberts (1983), Roberts & Peregrine (1983) and Bryant (1985). Such patterns have in turn been demonstrated to be unstable to infinitesimal perturbations in deep water by Ioualalen & Kharif (1994) (see also Badulin *et al.* 1995; Kimmoun, Ioualalen & Kharif 1999*b*), as well as in finite depth by Ioualalen, Roberts & Kharif (1996) and Ioualalen, Kharif & Roberts (1999). Of these, the deep-water analyses are perhaps of the most fundamental importance, as they pertain to fully dispersive waves in the open ocean. Short-crested wave patterns in deep water have also been studied experimentally by Kimmoun, Branger & Kharif (1999*a*), who found that some experiments with high steepness were affected by modulational instabilities. Hammack, Henderson & Segur (2005) also discussed instabilities in connection with their short-crested wave experiments, though many of their observed unsteady features have since been explained as generational effects (see Fuhrman & Madsen 2006; Henderson, Patterson & Segur 2006).

The aim of the present work is to study the relatively long-term fully nonlinear evolution of lowest-order short-crested wave instabilities (i.e. those involving resonant quartet interactions) in deep water via direct numerical simulation. The numerical model used is based on the highly accurate fully nonlinear Boussinesq-type formulation of Madsen *et al.* (2002) and Madsen, Bingham & Schäffer (2003), using the efficient finites difference solutions of Fuhrman & Bingham (2004). There is a need for such an investigation, as (to our knowledge) numerical simulations involving the instability of initially three-dimensional progressive wavetrains are non-existent in the literature, even in a weakly nonlinear context. The simulations considered herein therefore provide a deeper understanding of the evolution of simple three-dimensional wave spectra. Note that the spectral evolution of ensemble random three-dimensional waves has been studied previously by Onorato *et al.* (2002) and Dysthe *et al.* (2003), demonstrating numerically the formation of the $\omega^{-4}$ power law.

As shown by, for example, Ioualalen & Kharif (1994), there are two types of possible quartet resonances involving short-crested wave patterns, deemed to be of so-called class Ia and Ib, both of which will be considered here. The present study will focus primarily on the simulation of class Ia instabilities, which involve both components of the incident short-crested wave in the same resonant interaction. However, an example of a (computationally more demanding) class Ib instability will also be considered for completeness. As will be shown, the unstable evolution of these three-dimensional patterns is qualitatively different from that of initially plane waves.

The remainder of this paper is organized as follows. The Boussinesq-type model used throughout this numerical study is described briefly in § 2. A series of simulations involving classical two-dimensional class I instabilities, used primarily for validation and comparative purposes, are first provided in § 3. Simulations of short-crested wave instabilities are then considered in § 4, with class Ia and Ib instabilities respectively covered in §§ 4.2 and 4.3. The various results are discussed in § 5, with conclusions drawn in § 6.

## 2. The numerical model

The numerical model used in the present work is based on the fully nonlinear, high-order Boussinesq-type formulation of Madsen *et al.* (2002, 2003). This method uses exact representations of the kinematic and dynamic free-surface conditions expressed in terms of surface quantities as

$$\frac{\partial \eta}{\partial t} = \tilde{w}\,(1 + \nabla\eta \boldsymbol{\cdot} \nabla\eta) - \tilde{\boldsymbol{U}} \boldsymbol{\cdot} \nabla\eta, \tag{2.1}$$

$$\frac{\partial \tilde{\boldsymbol{U}}}{\partial t} = -g\nabla\eta - \nabla\left(\frac{\tilde{\boldsymbol{U}} \boldsymbol{\cdot} \tilde{\boldsymbol{U}}}{2} - \frac{\tilde{w}^2}{2}(1 + \nabla\eta \boldsymbol{\cdot} \nabla\eta)\right), \tag{2.2}$$

where $\tilde{\boldsymbol{U}} = (\tilde{U}, \tilde{V}) = \tilde{\boldsymbol{u}} + \tilde{w}\nabla\eta$. Here $\tilde{\boldsymbol{u}} = (\tilde{u}, \tilde{v}) = \boldsymbol{u}(\boldsymbol{x}, \eta, t)$ and $\tilde{w} = w(\boldsymbol{x}, \eta, t)$ are the horizontal and vertical velocities directly on the free surface $z = \eta$, $g = 9.81\,\mathrm{m\,s^{-2}}$ is the acceleration due to gravity, $\nabla = (\partial/\partial x, \partial/\partial y)$ is the horizontal gradient operator, and $t$ is time. The vertical distribution of fluid velocity is approximated via a Padé-enhanced truncated series solution of the Laplace equation, corresponding to

$$\boldsymbol{u}(\boldsymbol{x}, z, t) = (1 - \alpha_2\nabla^2 + \alpha_4\nabla^4)\hat{\boldsymbol{u}}^*(\boldsymbol{x}, t) + ((z - \hat{z})\nabla - \beta_3\nabla^3 + \beta_5\nabla^5)\hat{w}^*(\boldsymbol{x}, t), \tag{2.3}$$

$$w(\boldsymbol{x}, z, t) = (1 - \alpha_2\nabla^2 + \alpha_4\nabla^4)\hat{w}^*(\boldsymbol{x}, t) - ((z - \hat{z})\nabla - \beta_3\nabla^3 + \beta_5\nabla^5)\hat{\boldsymbol{u}}^*(\boldsymbol{x}, t), \tag{2.4}$$

where $\boldsymbol{x} = (x, y)$ and

$$\left.\begin{aligned} \alpha_2 &= \frac{(z-\hat{z})^2}{2} - \frac{\hat{z}^2}{18}, & \alpha_4 &= \frac{(z-\hat{z})^4}{24} - \frac{\hat{z}^2(z-\hat{z})^2}{36} + \frac{\hat{z}^4}{504}, \\ \beta_3 &= \frac{(z-\hat{z})^3}{6} - \frac{\hat{z}^2(z-\hat{z})}{18}, & \beta_5 &= \frac{(z-\hat{z})^5}{120} - \frac{\hat{z}^2(z-\hat{z})^3}{108} + \frac{\hat{z}^4(z-\hat{z})}{504}. \end{aligned}\right\} \tag{2.5}$$

Optimal velocity distributions are obtained with the expansion point near $\hat{z} = -h/2$, and we adopt this value throughout. Considering (2.3) and (2.4) at the sea bottom $z = -h$, the kinematic bottom condition (neglecting bottom slope) becomes

$$\left(1 - \tfrac{4}{9}\gamma^2\nabla^2 + \tfrac{1}{63}\gamma^4\nabla^4\right)\hat{w}^* + \left(\gamma\nabla - \tfrac{1}{9}\gamma^3\nabla^3 + \tfrac{1}{945}\gamma^5\nabla^5\right)\hat{\boldsymbol{u}}^* = 0, \tag{2.6}$$

where $\gamma = (h + \hat{z}) = h/2$. It is straightforward to include variable depth terms; however, as the present work is restricted to flat bottoms, they are not presented here. Analysis of this system has shown that it provides excellent linear and nonlinear properties to (wavenumber times depth) $kh \approx 25$, and accurate velocity kinematics to $kh \approx 12$, largely eliminating any shallow-water limitations conventionally associated with Boussinesq-type methods. Thus, over a large range of $kh$, the system may be regarded as a highly accurate approximation to the exact Laplace problem for nonlinear water waves.

The system of PDEs is solved numerically using the high-order (37-point) finite-difference spatial discretizations originally presented by Fuhrman & Bingham (2004), combined with the fifth-order six-stage explicit Runge–Kutta time-stepping scheme of Cash & Karp (1990). Closed (slip) boundary conditions are imposed on the exterior domain. Specifically, this corresponds to setting $\partial\eta/\partial x = 0$, $\partial^m u/\partial x^m = 0$, $\partial^n v/\partial x^n = 0$ and $\partial^n w/\partial x^n = 0$ at $x$-boundaries; and $\partial\eta/\partial y = 0$, $\partial^n u/\partial y^n = 0$, $\partial^m v/\partial y^m = 0$ and $\partial^n w/\partial y^n = 0$ at $y$-boundaries; where $m = 0, 2, 4$ and $n = 1, 3, 5$. These are implemented by simply reflecting the variables evenly (for odd derivatives) or oddly (for even derivatives) about the respective boundaries.

The discretization results in a numerical scheme that is, in principle, non-dissipative, which can be shown through standard linear Fourier analysis. However, weak dissipation is added in the form of a tenth-order (109-point, octagon shaped) Savitzky & Golay (1964) type smoothing filter, applied incrementally (after every $n_s$ time steps), which is generally necessary to remove (unphysical) high-wavenumber disturbances arising from the discretization of the nonlinear terms. In some cases, the filter additionally serves to prevent a computational breakdown when the waves are near breaking. In such instances (which will be clearly identified), wave breaking is thus prevented. A Fourier analysis of the filter is provided in the Appendix, which quantitatively demonstrates that its dissipative effects are primarily restricted to high wavenumber modes.

As shown by Fuhrman & Bingham (2004), the dominant computational expense of the model involves the iterative solution of an ill-conditioned sparse matrix problem, and simulations presented here use the matrix-free Fourier space preconditioner (within the GMRES algorithm of Saad & Schultz 1986) and irrotational operators, as discussed therein.

In all simulations, a perturbed incident wavefield is spread across the entire model domain as initial conditions, removing any potential background noise from an initial wavefront. These same conditions are then repeated indefinitely within a wavemaker region (relaxed over 65 grid-points) at the left-hand boundary, with $x = 0$ defined as the end of the wavemaker region. Additionally, a 100 grid-point sponge layer is placed at the right-hand boundary to absorb the outgoing wavefield. This works by simply multiplying the computed values after each time step by a decay function of the form $1 - (\exp(x_r^\mu) - 1)/(\exp(1) - 1)$, where $x_r$ is a scaled $x$-coordinate (uniformly increasing from 0 at the start of the sponge layer to 1 at the end), and where the relaxation coefficient is taken as $\mu = 3.5$. All simulations are run for a sufficient length of time to ensure that the energy (travelling roughly at the group velocity of the primary wavetrain) has propagated the full length of the numerical basin, after which the harmonic evolution effectively reaches a steady state.

## 3. Simulation of class I plane wave instabilities

We will begin this numerical study by first considering simulations of class I plane wave instabilities, whose evolution has been extensively studied in the literature. These simulations will aid in the interpretation of the short-crested simulations to be presented in §§4.2 and 4.3, while also serving as validation of the current model on a closely related phenomenon.

### 3.1. *Model set-up*

These simulations use numerically exact plane progressive incident waves computed from the method of Fenton (1988), having angular frequency $\omega_0$, crest-to-trough waveheight $H$ $(= 2a)$, wavelength $L_x = 2\pi/k$, wavenumber vector $\boldsymbol{k}_0 = (k, 0) =$

$(1,0)\,\mathrm{m}^{-1}$, and dimensionless depth $kh = 2\pi$. The generated carrier waves have a peak at $x = 0$ at $t = 0$. The perturbation frequencies and wavenumbers are chosen to excite the dominant class I instability based on the (deep water) method of McLean (1982*b*). Thus, to excite the desired instability, two perturbations of the form

$$\eta'_a = \frac{\epsilon H}{2}\sin(k_a x - \omega_a t), \tag{3.1}$$

$$\tilde{u}'_a = \frac{\epsilon\sqrt{g k_a} H}{2}\sin(k_a x - \omega_a t)\exp(k_a\eta), \tag{3.2}$$

$$\tilde{w}'_a = -\frac{\epsilon\sqrt{g k_a} H}{2}\cos(k_a x - \omega_a t)\exp(k_a\eta), \tag{3.3}$$

are superimposed over the corresponding base variables, with $\tilde{U}'_a = \tilde{u}'_a + \tilde{w}'_a\eta_x$, each with relative strength $\epsilon = 0.02$. The second perturbation has the same form as in (3.1)–(3.3), but with subscript $b$. This corresponds to a uni-directional variant of the wavemaker conditions used previously in Fuhrman *et al.* (2004). While these simulations are, in principle, two-dimensional, they are still simulated using two horizontal dimensions (on a $8193 \times 17$ grid), with resolution $\Delta x = L/32$, $\Delta t \approx T/32$, and smoothing interval $n_s = 32$, matching the set-up used in the forthcoming short-crested wave simulations.

The perturbation wavenumber vectors are defined as

$$\boldsymbol{k}_a = (k_a, 0) = (1 + p, q)k, \qquad \boldsymbol{k}_b = (k_b, 0) = (1 - p, -q)k, \tag{3.4}$$

with $q = 0$, while the perturbation frequencies are defined in terms of a single parameter $\delta$, such that they are centred about the primary frequency $\omega_0$

$$\omega_a = (1 + \delta)\omega_0, \qquad \omega_b = (1 - \delta)\omega_0. \tag{3.5}$$

Here, $\delta$ is computed as

$$\delta = p + \mathrm{Re}\{\sigma\}\frac{\sqrt{gk}}{\omega_0}, \tag{3.6}$$

with $\sigma$ the corresponding eigenvalue from the method of McLean (1982*b*), representing a dimensionless complex frequency in a frame of reference moving with the primary wave. As can be seen from (3.5), the perturbation waves with subscript $a/b$ correspond to unstable upper/lower side-bands of the primary wave. Chosen in this manner, the perturbation waves in conjunction with the primary wave satisfy the quartet resonance conditions

$$2\omega_0 = \omega_a + \omega_b, \tag{3.7}$$

$$2\boldsymbol{k}_0 = \boldsymbol{k}_a + \boldsymbol{k}_b. \tag{3.8}$$

It should finally be mentioned that, as shown by McLean (1982*a*), a finite depth can, in fact, cause the dominant class I instability to become three-dimensional. Indeed, even with the relatively large dimensionless depth $kh = 2\pi$ used here, we have found (from our own implementation of McLean's finite-depth analysis) that the dominant class I instability is, in fact, slightly three-dimensional for roughly $ak \leqslant 0.107$ (this matches reasonably with figure 6 of Trulsen & Dysthe 1996). However, as our intention is to approximate a deep-water problem in a single horizontal dimension (both for comparison against previous deep-water studies, and for later contrast with short-crested simulations in two-horizontal dimensions), we will base our model inputs on the deep-water analysis of McLean (1982*b*), as described above.

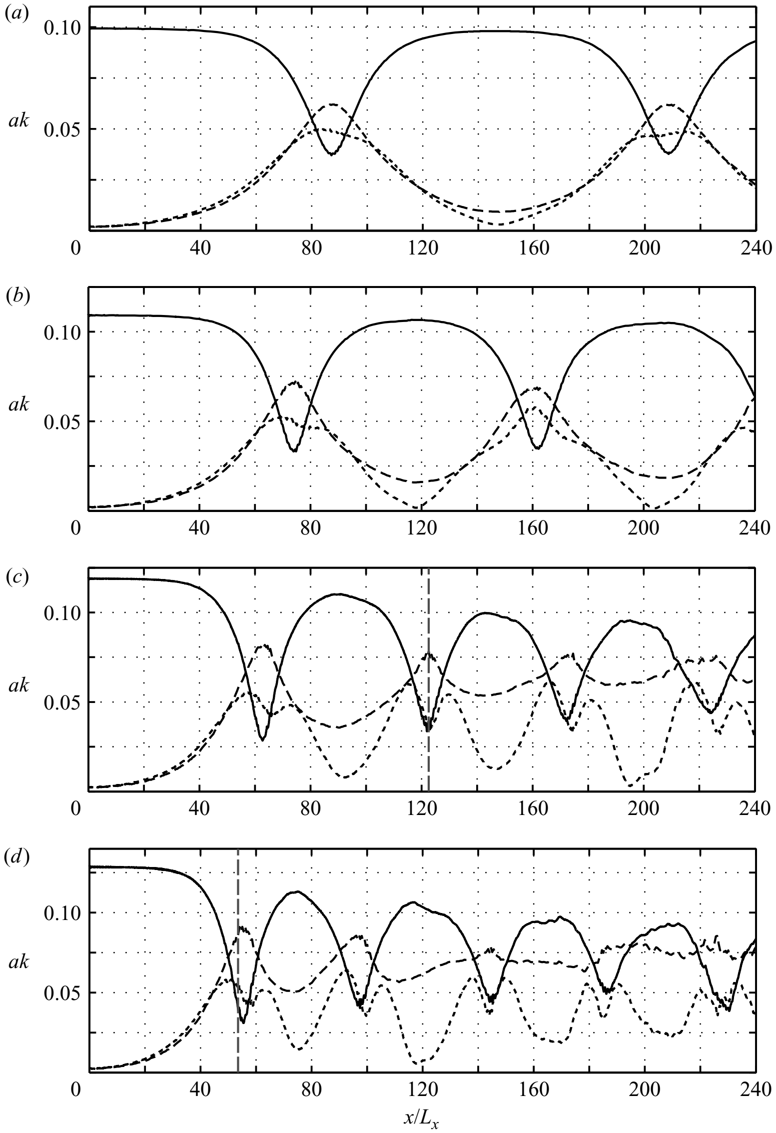

FIGURE 1. Computed evolution of the primary frequency (full line) and lower/upper side-bands (long/short dashed lines) from simulations of class I plane wave instabilities with $\epsilon = 0.02$ and (*a*) $ak = 0.10$, (*b*) 0.11, (*c*) 0.12, (*d*) 0.13. The simulations correspond to dominant instabilities based on the method of McLean (1982*b*) with (*a*) $(p, q) = (0.18, 0)$, $\sigma = -0.0880 + 0.00408\mathrm{i}$; (*b*) $(p, q) = (0.19, 0)$, $\sigma = -0.0924 + 0.00485\mathrm{i}$; (*c*) $(p, q) = (0.20, 0)$, $\sigma = -0.0968 + 0.00565\mathrm{i}$; (*d*) $(p, q) = (0.22, 0)$, $\sigma = -0.1059 + 0.00650\mathrm{i}$. The dashed vertical lines in (*c*) and (*d*) indicate the estimated breaking location.

### 3.2. *Computed results*

The computed evolution of the primary $\omega_0$ and upper/lower side-band frequencies $\omega_a/\omega_b$ from a series of class I simulations having initial steepness $ak = 0.10$, 0.11, 0.12, and 0.13 are provided in figure 1, with the precise $(p, q)$ and $\sigma$ values as indicated in the caption. These results are best viewed within the context of the

| $ak$ | Class I | Class Ia | Class Ib |
|---|---|---|---|
| 0.08 | — | 0.19 | — |
| 0.09 | — | 0.24 | — |
| 0.10 | 0.31 | 0.26 | — |
| 0.11 | 0.42 | 0.37 | — |
| 0.12 | 0.62 | — | — |
| 0.125 | 0.61 | 0.49 | — |
| 0.13 | 0.74 | — | — |
| 0.15 | — | 0.67 | — |
| 0.20 | — | 1.61 | 0.79 |

TABLE 1. Computed maximum forward surface slopes (i.e. $\max(-\eta_x)$) for simulations of class I plane wave instabilities (from § 3), as well as class Ia and Ib short-crested-wave instabilities (from § 4). These are computed using first-order difference approximations along $y=0$ over the final 600 times steps. Note that results from some class Ia simulations not specifically discussed in § 4.2 are included here for completeness.

earlier class I breaking threshold steepness studies of Banner & Tian (1998) and Henderson, Peregrine & Dold (1999). Specifically, we will here consider their results with constant $p=0.20$ (equivalent to their 5 waves in one modulation), which is nearest to the theoretically dominant $p$ values used in the current simulations (in the range $0.18 \leqslant p \leqslant 0.22$). Figures 1 and 2 of Banner & Tian (1998) indicate that for $p=0.20$ (their $N=5$), the unstable evolution with $ak=0.11$ leads to a recurrence cycle, whereas an increase to $ak=0.1125$ leads to breaking. Figure 1 of Henderson *et al.* (1999) similarly predicts recurrence with $ak=0.11$ and breaking with $ak=0.12$ (see also Dold & Peregrine 1986). Our computed results are generally consistent with these earlier studies. Below the threshold $ak=0.1125$, as illustrated in figures 1(*a*) and 1(*b*) (with $ak=0.10$ and 0.11), the simulations lead to a nearly symmetric recurrence cycle, widely established as the correct evolution in weakly nonlinear cases. Above this threshold, where dissipative breaking would be physically expected, the simulations lead to an asymmetric evolution, characterized by a permanent transfer of energy to the lower side-band, which is apparent in both figures 1(*c*) and (*d*) (respectively, with $ak=0.12$ and 0.13).

To characterize the local steepness of the developed wavefields, the maximum computed forward surface slopes (i.e. $\max(-\eta_x)$) from these simulations are provided in the second column of table 1. These will be used to formulate an approximate (empirical) breaking criterion, to be used throughout this work. Also provided in table 1 are computed values from simulations of class Ia and Ib short-crested wave instabilities, to be discussed in § 4. Here, it is noteworthy that for the class I simulation with $ak=0.12$ (i.e. slightly above the previously mentioned breaking threshold steepness) the maximum computed surface slope matches the threshold $\tan(32^\circ)\approx 0.62$ used in the wave-breaking model of Sørensen, Madsen & Schäffer (1998), providing confidence that the computed surface slopes are indeed reasonably indicative of a breaking event. A similar simulation with $ak=0.125$ (and $p=0.21$, not specifically shown here) results in a slightly lower value of 0.61. Based on these values, we will estimate the location of incipient wave breaking as the point where the forward surface slope first exceeds the empirical threshold 0.61. These locations are marked by vertical dashed lines in figures 1(*c*) and 1(*d*), which are both seen to immediately precede the observed permanent separation of the side-bands.

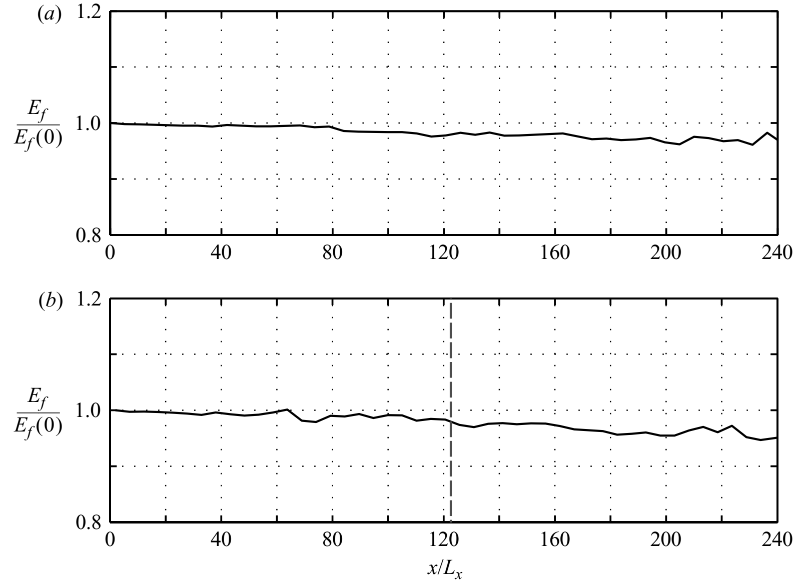

FIGURE 2. Computed relative mean energy flux over an approximate group period from simulations of class I plane wave instabilities with (a) $ak = 0.11$ and (b) 0.12. The vertical dashed line in (b) marks the estimated breaking location.

To quantify the numerical dissipation introduced from the filtering in these simulations, we estimate the mean energy flux $E_f$ at points along the domain by

$$E_f = \frac{1}{T_g} \int_t^{t+T_g} \int_{-h}^{\eta} (p^+ u)\, \mathrm{d}z\, \mathrm{d}t, \tag{3.9}$$

where the group period is taken as $T_g = T/\delta$, rounded to the nearest time step, with $T = 2\pi/\omega_0$ the period of the primary wave. This computation first requires the numerical evaluation of the velocity profiles via (2.3) and (2.4), with the excess (dynamic) pressure $p^+$ then computed from the integrated vertical Euler equation. It should be noted that the higher-order term $\rho(u^2 + w^2)u/2$ (from the exact expression for the energy flux, with $\rho$ the fluid density) has been omitted within the double integral in (3.9). We have found that this makes little difference at locations where the waves are de-modulated, while reducing the sensitivity of the computation to apparent numerical errors in the fifth-derivatives when the waves are very steep.

The computed (relative) mean energy flux for $ak = 0.11$ and 0.12 (i.e. both below and above the breaking threshold steepness) are presented in figure 2. As mentioned previously, a Fourier analysis of the tenth-order smoothing filter used throughout this work is provided in the Appendix, which shows that the associated dissipative effects are primarily restricted to rather high wavenumber modes. These effects should therefore be expected to become most important in the vicinity of steep wave events. This is generally supported by figure 2, which shows decreases in the mean energy flux occurring in a loosely step-like fashion along the domain. From figure 2, we estimate that the flux of energy in both cases is conserved to within roughly 2 % through the first recurrence cycle, and to within approximately 3 % through the second. With $ak = 0.12$, the flux of energy is conserved to within 5 % over the length of the domain. We have found reasonably similar results for the other cases.

While their qualitative behaviour differs considerably (see again figures 1*b* and 1*c*), the energy losses in these two cases are, in fact, quite similar. This is not altogether surprising, given the relatively small difference in the incident wave steepnesses. We emphasize, however, that the recurrent results below the breaking threshold are not sensitive to the precise level of smoothing. For example, an otherwise identical simulation with $ak = 0.11$, where the smoothing frequency is increased to every $n_s = 1$ time steps (i.e. an application 32 times more frequent), leads to essentially the same evolution as depicted in figure 1(*b*). Moreover, simulations with less smoothing ($n_s = 64$) similarly lead to the same evolution with $ak = 0.11$, but to a computational breakdown with $ak = 0.12$, which we find is typical of breaking cases. Thus, for the simulated class I cases with $ak \geqslant 0.12$, it is our interpretation that high-wavenumber dissipation from the smoothing filter prevents wave breaking, and is responsible for the observed asymmetric evolution.

When viewed in this context, these results are consistent with numerous other numerical studies (e.g. Trulsen & Dysthe 1990; Hara & Mei 1991; Skandrani, Kharif & Poitevin 1996) as well as physical experiments (e.g. Melville 1982; Tulin & Waseda 1999), which have found that the frequency downshift phenomenon (within class I plane wave instabilities) is caused by combined nonlinearity and dissipation (either from breaking, wind effects, or viscosity and surface tension). These simulations convincingly demonstrate that, while the smoothing filter apparently serves as the dissipative mechanism promoting a permanent transfer of energy to the lower sideband for sufficiently steep waves, it does not artificially promote this phenomenon at lower values of the wave steepness. As will be seen, it is important to establish that the model properly predicts this particular behaviour, as it will become highly relevant in the forthcoming simulations of short-crested wave instabilities.

We finally note that the results presented here are also consistent with the work of Madsen *et al.* (2002), who considered reasonably similar class I simulations (using the same Boussinesq-type model, but in a single horizontal dimension) with incident steepness $ak = 0.10$, 0.105 and 0.133. These lead to qualitatively similar evolutions, with simulations at low steepness ($ak = 0.10$ and 0.105) leading to recurrence, and with the case of $ak = 0.133$ demonstrating good agreement (before, as well as after the reported region of physical breaking) with the measured frequency downshift of Tulin & Waseda (1999), as indicated in their figure 15*b*. In these simulations, wave breaking was similarly prevented by high-wavenumber dissipation from a smoothing filter. Thus, while this methodology does not model wave breaking in any physical sense (the actual level of dissipation is probably underestimated), there is evidence that results computed in this manner are still qualitatively useful, indicative of the continued evolution after a dissipative steep-wave event. They will therefore continue to be presented throughout the present work, with the estimated location of incipient breaking clearly marked when it is relevant.

## 4. Simulation of short-crested wave instabilities

Having established the model accuracy in simulating two-dimensional class I instabilities, we will now turn our attention to the simulation of three-dimensional short-crested wave instabilities, which is the primary focus of the present work.

### 4.1. *Model set-up*

The basic model set-up now uses the steady third-order short-crested wave solution of Hsu *et al.* (1979) as the incident wave, which has been transformed from dimensionless to dimensional quantities. This solution is comprised of the two primary wavenumber vectors

$$\boldsymbol{k}_{01} = (k_x, k_y), \qquad \boldsymbol{k}_{02} = (k_x, -k_y), \tag{4.1}$$

both having angular frequency $\omega_0$. All simulations are normalized using the wavenumber modulus $k=\sqrt{k_x^2+k_y^2}=1\ \mathrm{m}^{-1}$, with dimensionless depth $kh=2\pi$, i.e. deep water, maintaining the same parameters as in § 3. These short-crested solutions will be characterized by the wave steepness $ak$, where $a$ is again defined as half the total crest-to-trough waveheight, and the angle $\theta$ such that

$$(k_x, k_y) = (\sin\theta, \cos\theta)k. \tag{4.2}$$

Thus, $\theta=0°$ and 90°, respectively, correspond to the standing and plane short-crested wave limits.

Instabilities are excited within the model by superimposing two short-crested perturbation waves of the form

$$\eta_a' = \epsilon a_1 \cos(\omega_a t - k_{ax}x)\cos(k_{ay}y), \tag{4.3}$$

$$\tilde{U}_a' = \epsilon a_1 \omega_a \frac{k_{ax}}{k_a}\frac{\cosh k_a(h+\eta)}{\sinh k_a h}\cos(\omega_a t - k_{ax}x)\cos(k_{ay}y), \tag{4.4}$$

$$\tilde{V}_a' = \epsilon a_1 \omega_a \frac{k_{ay}}{k_a}\frac{\cosh k_a(h+\eta)}{\sinh k_a h}\sin(\omega_a t - k_{ax}x)\sin(k_{ay}y), \tag{4.5}$$

over the corresponding base variables, each with relative strength $\epsilon$. Here $k_a=\sqrt{k_{ax}^2+k_{ay}^2}$, while $a_1$ is the amplitude of the first-order primary wave component from the third-order solution of Hsu *et al.* (1979). The second perturbation wave has the same form as that in (4.3)–(4.5), with subscript $b$. The short-crested perturbation wavefield therefore consists of the four wavenumber vectors

$$\boldsymbol{k}_{a1} = (k_{ax}, k_{ay}), \qquad \boldsymbol{k}_{a2} = (k_{ax}, -k_{ay}), \tag{4.6}$$

$$\boldsymbol{k}_{b1} = (k_{bx}, k_{by}), \qquad \boldsymbol{k}_{b2} = (k_{bx}, -k_{by}), \tag{4.7}$$

with each short-crested wave again having equal $x$-components, with opposite $y$-components. The determination of these perturbation components will be made clear in the following subsections.

### 4.2. *Simulation of class Ia short-crested wave instabilities*

Ioualalen & Kharif (1994) demonstrate in their analysis that for low to moderate wave steepness, and relatively large (or sufficiently small) $\theta$, the dominant short-crested wave instability is of so-called class Ia. Specifically, they present instability diagrams for short-crested waves with incident angle $\theta=80°$ and steepness $ak=0.10$ and 0.20 in their figure 8. These are presented in the traditional $(p, q)$-plane, where $p$ and $q$, respectively, govern the perturbation wavenumbers in the propagating and transverse directions, in a manner to be described. From this figure, we estimate the dominant instabilities for these cases to occur at $(p, q)=(0.16, 0)$ and $(0.275, 0)$, respectively. Based on these two values, combined with the third constraint that $p=0$ when $ak=0$, the dominant $p$ values for other steepnesses considered are estimated through the empirical second-order polynomial

$$p = 1.825ak - 2.25(ak)^2. \tag{4.8}$$

| Class | $ak$ | $\theta$ (deg.) | $(k_x, k_y)/k$ | $\omega_0$ ($\mathrm{s}^{-1}$) | $(p, q)$ | $\delta$ | $\epsilon$ |
|---|---|---|---|---|---|---|---|
| Ia | 0.10 | 80 | (0.984,0.174) | 3.144 | (0.16,0) | 0.0806 | 0.02 |
| Ia | 0.125 | 80 | (0.984,0.174) | 3.150 | (0.193,0) | 0.0954 | 0.02 |
| Ia | 0.15 | 80 | (0.984,0.174) | 3.159 | (0.223,0) | 0.117 | 0.02 |
| Ia | 0.20 | 80 | (0.984,0.174) | 3.185 | (0.275,0) | 0.149 | 0.02 |
| Ib | 0.20 | 60 | (0.866,0.5) | 3.161 | (0.173,0.1) | 0.111 | 0.10 |

TABLE 2. Summary of parameters used for the simulation of various short-crested wave instabilities. Each case approximately matches the dominant instability based on the analysis of Ioualalen & Kharif (1994).

This leads to the values given in table 2, which provides a summary of the parameters used in each of the short-crested wave simulations considered in this work. A more precise variation of dominant $p$ values versus $ak$ has not been tabulated or plotted in the liturature, hence this approach seems a reasonable and systematic means for obtaining the input values for the purposes of the present numerical study. As can be seen in table 2, each of the simulations for the class Ia instabilities uses a relatively small relative perturbation strength $\epsilon = 0.02$, similar to § 3, approximating an infinitesimal disturbance.

To promote a class Ia short-crested wave instability, the perturbation wavenumber components are defined as

$$(k_{ax}, k_{ay}) = (\sin\theta + p, \cos\theta + q)k, \tag{4.9}$$

$$(k_{bx}, k_{by}) = (\sin\theta - p, \cos\theta + q)k, \tag{4.10}$$

with corresponding perturbation frequencies $\omega_a$, $\omega_b$ defined as in (3.5). The value of $\delta$ could, in principle, be obtained directly from the real part of the eigenvalues $\sigma$ from the stability analysis of Ioualalen & Kharif (1994), similar to (3.6). Unfortunately, they only report the imaginary parts in the analysis (corresponding to the strength of the instability). We have therefore opted to determine the parameter $\delta$ directly from the model, by locating the side-band peaks from Fourier analyses of time series (from preliminary simulations) at points sufficiently far from the wavemaker to have been affected only by the initial wavenumber disturbance. This leads to the values given in table 2.

The perturbation waves, in conjunction with the primary short-crested wave, are now seen to satisfy two quartet resonant interactions

$$\boldsymbol{k}_{01} + \boldsymbol{k}_{02} = \boldsymbol{k}_{a1} + \boldsymbol{k}_{b2}, \qquad \boldsymbol{k}_{01} + \boldsymbol{k}_{02} = \boldsymbol{k}_{b1} + \boldsymbol{k}_{a2}, \tag{4.11}$$

both in conjunction with (3.7). Each of these interactions involves the resonance of both primary short-crested wave components with a single component from both perturbation waves $a/b$. The wavenumber vectors in (4.11) are again as defined in § 4.1. As noted previously, the dominant class Ia instabilities conveniently have $q = 0$, which from (4.2), (4.9) and (4.10) means that $k_{ay} = k_{by} = k_y$. This is a special case, particularly attractive for numerical simulation with the present model, since through symmetry about the side-walls, the computational domain need only consist of a single half transverse wavelength. This might also make them the most easily observed experimentally, as the side-walls (of a finite width tank) can govern the selection of the transverse instability as discussed, e.g. by Fuhrman & Madsen (2005), within the context of class II plane wave instabilities.

| Class | $ak$ | Grid | $L_x/\Delta x$ | $L_y/\Delta y$ | $T/\Delta t$ | $n_s$ | Time steps | CPU (h) |
|---|---|---|---|---|---|---|---|---|
| Ia | 0.10 | $8193 \times 17$ | 32 | 32 | 31.9 | 32 | 20 000 | 164 |
| Ia | 0.125 | $8193 \times 17$ | 32 | 32 | 31.9 | 32 | 20 000 | 185 |
| Ia | 0.15 | $8193 \times 17$ | 32 | 32 | 31.8 | 32 | 20 000 | 211 |
| Ia | 0.20 | $4097 \times 17$ | 32 | 32 | 31.5 | 4 | 10 000 | 60 |
| Ib | 0.20 | $2049 \times 65$ | 25 | 25.6 | 31.8 | 8 | 7 000 | 93 |

TABLE 3. Computational summary for the simulations of short-crested wave instabilities. All simulations use $k = 1$ m$^{-1}$ and $\Delta t = 0.0626$ s, with period $T = 2\pi/\omega_0$.

A computational summary of the various short-crested simulations considered in this work is provided in table 3, which includes the size of the domain, the spatial/temporal resolution, the smoothing interval $n_s$, the number of time steps, as well as the required CPU time for each case. All simulations have been run on a single 3.2 GHz Pentium 4 processor, with 2 GB RAM. Here it can be seen that the various simulations are computationally demanding, with the longest simulation requiring nearly 9 days. These demands could probably, in some cases, be reduced via the use of periodic boundaries. We prefer the use of a long domain when possible, however, as it is more physically realistic, having the near physical equivalent of an experimental wavetank. Accordingly, the current generation method permits the introduction of longitudinal perturbation wavenumbers that are not necessarily an exact fraction of the primary wave, while also allowing any wavenumbers corresponding to a given frequency to adjust naturally (owing to amplitude dispersion) along the tank. Moreover, these simulations also demonstrate applications of the present fully nonlinear method on large computational domains, approaching sizes of interest for practical engineering problems. If future comparisons with periodic boundaries are desired, however, it is commonplace to convert the evolution in space to time using $t = x/c_g$, where $c_g$ is the group velocity of the primary wavetrain.

The computed harmonic amplitudes of the primary wave $\omega_0$ and the upper/lower side-band frequencies $\omega_a/\omega_b$ from the simulations of class Ia short-crested wave instabilities are shown in figure 3. The harmonic analyses are computed through linear-least-squares regression of time series at points along $y = 0$. The theoretical growth is also shown by the $\circ$ in figures 3(*a*) and 3(*d*), for the two cases where the precise $(p, q)$ values have been determined directly from the analysis of Ioualalen & Kharif (1994). The theoretical growth rates $\mathrm{Im}\{\sigma\}$ for these two cases have then been estimated from their figure 10. As can be seen, the growth of the perturbations near the inception in both cases matches closely with the theory, serving as validation for at least the initial stage of these simulations. At later stages, the computed growth slows compared to the theory in figure 3(*a*), leading to a quasi-recurrence cycle, while the theoretical growth is maintained almost exactly for the lower side-band in figure 3(*d*) to $x \approx 29L_x$.

From the weakly nonlinear cases depicted in figure 3(*a*) and 3(*b*) (respectively, with $ak = 0.10$ and 0.125), we observe a quasi-recurrence cycle, as was previously noted. The unstable evolution of these three-dimensional waves is, however, qualitatively different from the previously observed evolution of weakly nonlinear plane class I instabilities. The recurrence cycle observed in figures 3(*a*) and 3(*b*) is not symmetric: after the initial growth phase, the lower side-band maintains an amplitude larger than that of the upper. This is more pronounced for the case with larger steepness

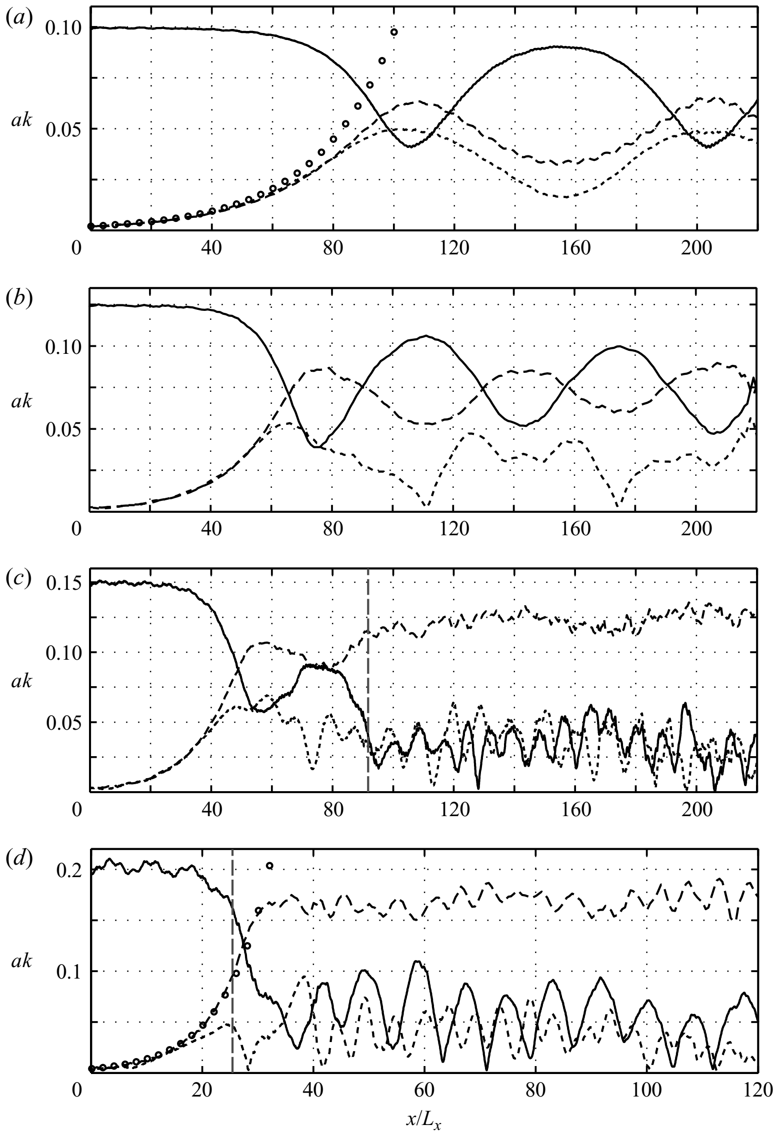

FIGURE 3. Computed evolution of the primary frequency (full line) and lower/upper side-bands (long/short dashed lines) from simulations of class Ia short-crested wave instabilities with $\epsilon = 0.02$, $\theta = 80^\circ$, and steepness (*a*) $ak = 0.10$, (*b*) 0.125, (*c*) 0.15, (*d*) 0.20. The circles in (*a*) and (*d*) indicate the theoretical exponential growth, given by $\epsilon a_1 \exp(\mathrm{Im}\{\sigma\}\sqrt{gk}x/c_g)$, where (*a*) $\mathrm{Im}\{\sigma\} = 0.0031$ and (*d*) 0.99. The dashed vertical lines in (*c*) and (*d*) indicate the estimated breaking locations.

$ak = 0.125$ (figure 3*b*), though the quasi-recurrence cycle is still evident for virtually the entire length of the computational basin. Based on the empirical breaking criterion from § 3, these class Ia cases with $ak \leqslant 0.125$ would not lead to physical breaking, as the maximum computed forward surface slopes given in table 1 are well below the previously determined threshold of 0.61. Note that additional testing has shown that similar simulations with even lower steepness (i.e. $ak \leqslant 0.10$, as given in table 1) lead

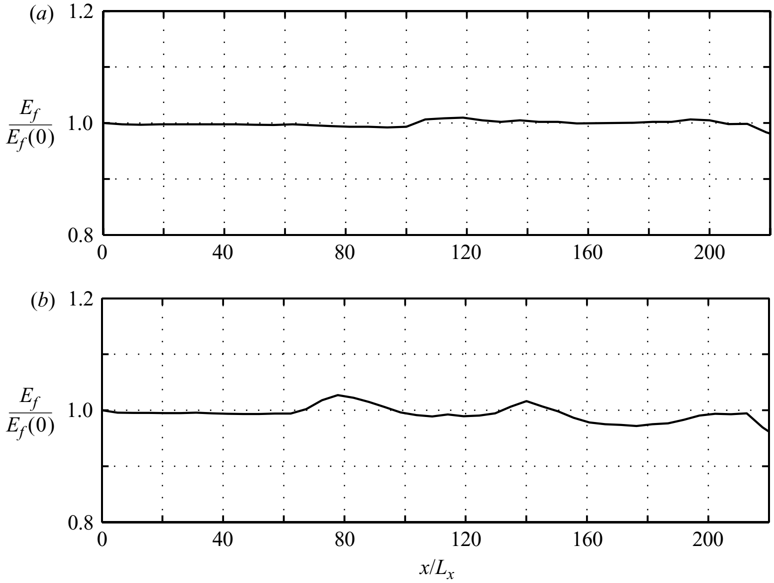

FIGURE 4. Computed relative mean energy flux over an approximate group period from simulations of class Ia short-crested wave instabilities with (*a*) $ak = 0.10$ and (*b*) 0.125.

to evolutions qualitatively similar to figure 3(*a*), though we do not present them here for brevity.

To quantify the energy losses due to the filtering in these simulations, the mean energy flux is again estimated along the domain via (3.9), which is now also integrated across the width of the computational domain. The results for the cases with $ak = 0.10$ and 0.125 are provided in figure 4 as examples. Figure 4(*a*) ($ak = 0.10$), demonstrates that the energy flux is conserved within 1 % through the first quasi-recurrence cycle, with no noticeable loss after the steepened region (the mean energy flux eventually levels to a value very near that at the wavemaker). Thus, the flux of energy is conserved better in this case than, for example, in figure 2(*a*), which is consistent with the smaller surface slopes encountered, see table 1. With $ak = 0.125$ (figure 4*b*) there are noticeable fluctuations in the computed energy flux during the region where the waves are steepened. Here, the flux of energy is conserved within roughly 3 % throughout the domain. Based on the relatively level values during the periods of de-modulation, we estimate a 1 % loss after the first quasi-recurrence cycle, with an additional 2 % loss through the second cycle. Thus, in this case, the flux of energy is conserved within roughly the same level as the class I plane wave cases considered earlier. In support of the demonstration in § 3 that the weak dissipation from the smoothing filter is not artificially promoting the observed behaviour, we note that otherwise identical simulations for the case with $ak = 0.10$ with significantly more ($n_s = 1$) and less smoothing ($n_s = 128$) lead to essentially the same evolution as depicted in figure 3(*b*). Moreover, refining the grid in either the $x$- or $y$-directions (with either $L_x/\Delta x = 64$ or $L_y/\Delta y = 64$, which pushes the dissipative effects from the filter to yet higher wavenumbers), also leads to the same behaviour as depicted here (this has been confirmed for both $ak = 0.10$ and 0.125). Thus, these results are insensitive to the filtering and resolution, and suggest that the observed asymmetric behaviour is part of the conservative (non-breaking) evolution of short-crested wave instabilities.

Alternatively, we expect that the simulated class Ia cases with $ak \geqslant 0.15$ (depicted in figures 3*c* and 3*d*) would lead to physical breaking, as the computed maximum surface slopes in table 1 significantly exceed the previously mentioned empirical threshold. This is further supported by grid refinement studies (using $\Delta x = L_x/64$) with $ak = 0.15$ and 0.20, which lead to a computational breakdown, even when the smoothing filter is applied after every $n_s = 2$ and 1 time steps, respectively. For these cases, the location of incipient breaking has been estimated as before in figures 3(*c*) and 3(*d*), again marked by the vertical dashed lines. In both cases this location coincides with a distinct qualitative shift in the evolution. In figure 3(*c*) this marks the break in the quasi-recurrence cycle, while in figure 3(*d*) this corresponds closely to the rapid decrease of the primary wave and upper side-band amplitudes. It therefore seems likely that these qualitative changes in the evolution are driven in part by the high-wavenumber dissipation of the smoothing filter (in combination with the large steepness of the waves), resulting in a permanent downshift of the peak frequency. We again stress that as wave breaking has not been physically modelled, the computed evolution beyond the onset of breaking should only be considered qualitatively. These results do suggest, however, that dissipation is important in breaking the quasi-recurrence cycle, resulting in the chaotic (i.e. disorderly) evolution of the primary frequency and upper side-band.

In all of the short-crested wave simulations, additional frequencies to those shown in figure 3 are important. This is illustrated in figure 5, which shows full spectra of Fourier amplitudes for each of the cases considered. In particular, it is seen that the transfer of energy to the lower side-band is accompanied by a similar transfer to more distant upper side-band frequencies. We find qualitatively similar results for the class Ia simulations with $ak \geqslant 0.15$ up to the estimated breaking point, which are then followed by a significant transfer to the more distant lower side-band frequencies. This can be seen, for example, in figures 5(*e*)–5(*h*), which show full spectra for the cases with $ak = 0.15$ and 0.20 before and after the estimated breaking locations. Note also that a similar growth in the more distant upper side-bands occurs in the class I plane wave simulations with $ak \leqslant 0.11$ (from § 3) in the regions where the peak frequency is temporarily downshifted.

To further characterize the spectral development in each of the class Ia cases considered, the spatial evolution of the mean frequency defined as

$$\overline{\omega} = \frac{\sum\limits_{m=1}^{M} \omega_m |a_m|^2}{\sum\limits_{m=1}^{M} |a_m|^2}, \tag{4.12}$$

is provided in figure 6 (normalized by the computed values just beyond the wavemaker region), with $M$ the number of discrete frequencies comprising the Fourier transform of time series along the domain. Figure 6 shows that with $ak = 0.10$ the mean frequency is practically constant along the domain, whereas with $ak = 0.125$ it becomes slightly upshifted during the periods of maximum modulation (owing to the previously noted energy transfer to more distant upper side-band frequencies). This is consistent with results of Trulsen & Dysthe (1997) who found a similar upshifting of the mean frequency in the context of three-dimensional class I plane wave instabilities. Alternatively, the breaking cases ($ak \geqslant 0.15$) result in a pronounced downshift in the mean frequency, beginning immediately after the estimated breaking locations. The marked differences seen in figure 6 further support that we have accurately distinguished between breaking and non-breaking cases.

To provide an indication of the physical appearance of the computed quasi-recurrent unstable class Ia short-crested wave evolution, segments of the computed

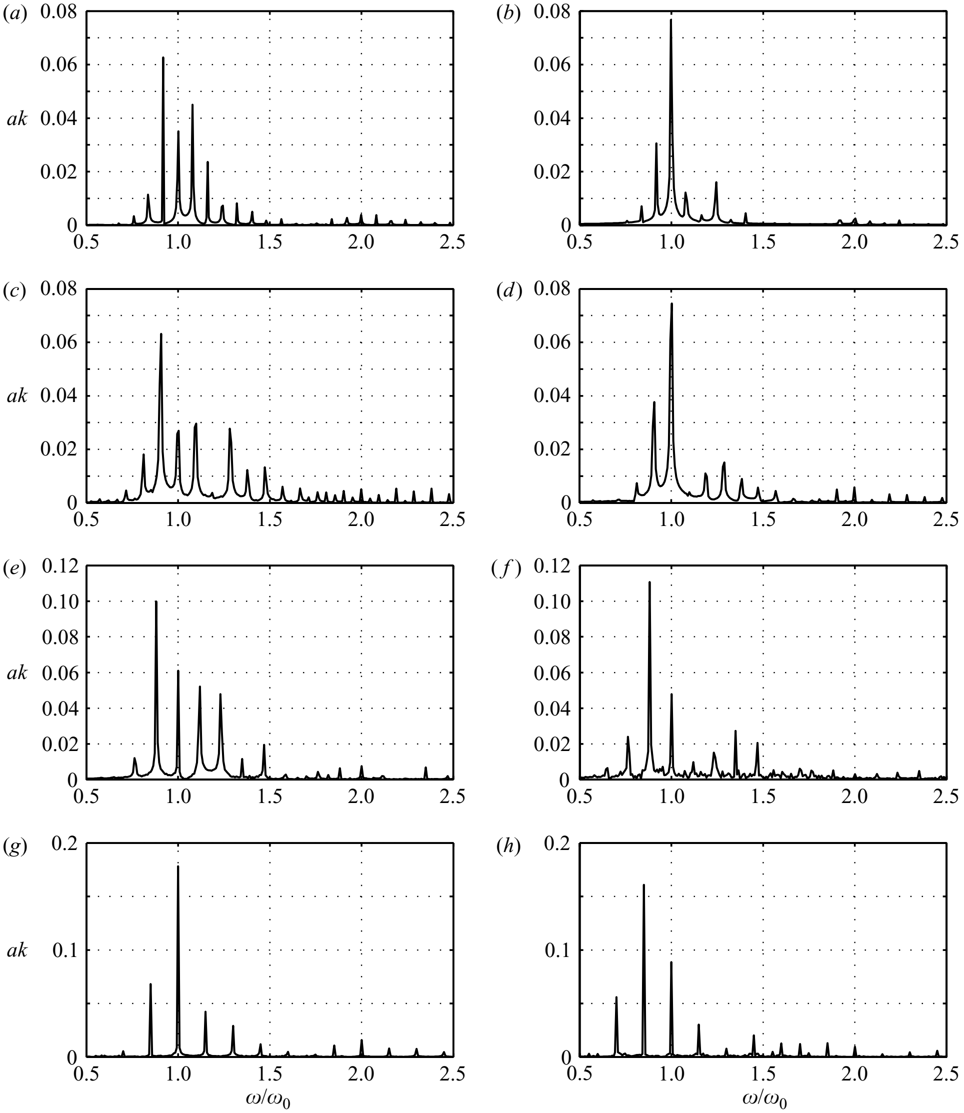

FIGURE 5. Computed spectra of Fourier amplitudes from the class Ia simulations with $(a, b)$ $ak = 0.10$ at $x \approx 104L_x/154L_x$, $(c, d)$ $ak = 0.125$ at $x \approx 73L_x/111L_x$, $(e, f)$ $ak = 0.15$ at $x \approx 61L_x/167L_x$, and $(g, h)$ $ak = 0.20$ at $x \approx 23L_x/51L_x$.

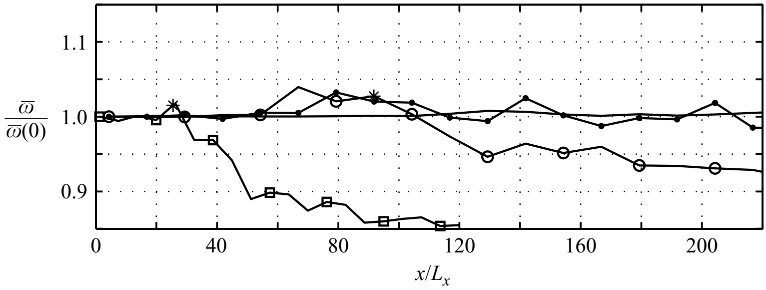

FIGURE 6. Computed evolution of the relative mean frequency for class Ia simulations with (full line) $ak = 0.10$, (line with dots) 0.125, (line with circles) 0.15, and (line with squares) 0.20. $*$, the estimated breaking locations for $ak = 0.15$ and 0.20.

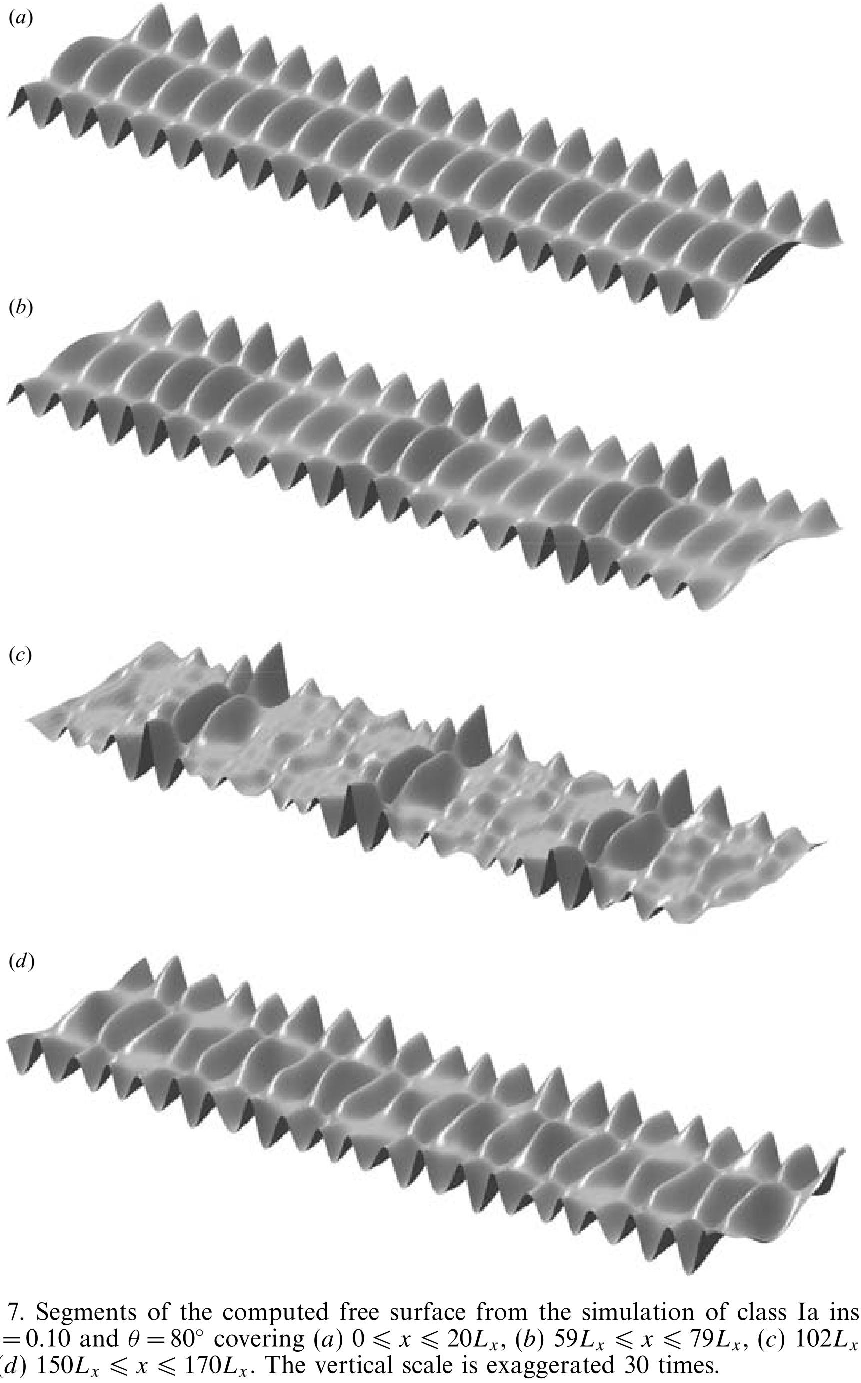

FIGURE 7. Segments of the computed free surface from the simulation of class Ia instability with $ak = 0.10$ and $\theta = 80^\circ$ covering (*a*) $0 \leqslant x \leqslant 20L_x$, (*b*) $59L_x \leqslant x \leqslant 79L_x$, (*c*) $102L_x \leqslant x \leqslant 122L_x$, (*d*) $150L_x \leqslant x \leqslant 170L_x$. The vertical scale is exaggerated 30 times.

free surface from the simulation with $ak = 0.10$ are shown in figure 7. Note that in this, as well as all other surface plots included herein, the free surface is reflected a single time across the $y$-axis, to cover at least a single full transverse wavelength. From this figure it is seen that the initially regular short-crested wave pattern, figure 7(*a*), eventually becomes modulated, as in figure 7(*b*). When the side-bands are near their respective peaks, figure 7(*c*), the wavetrain has almost completely focused into steep three-dimensional pulses. These eventually develop back to a reasonably regular short-crested wavetrain, as depicted in figure 7(*d*), resembling (though certainly not identical to) the incident short-crested waves. This evolution is in many ways analogous to the classical two-dimensional class I instability, though the recursion is again less complete.

A segment of the computed free surface for the steepest case with $ak = 0.20$ is similarly shown in figure 8, covering the region $0 \leqslant x \leqslant 40L_x$. Here the initially regular incident wavetrain again begins to develop into steepened three-dimensional pulses. Beyond the estimated breaking location (marked by the arrow), however, the appearance changes dramatically, with the free surface rapidly disintegrating into one that is rather irregular, which then persists to the end of the domain.

It must finally be mentioned, that additional testing has indicated that the precise evolution for a given steepness is somewhat sensitive to the chosen value for $p$ (or equivalently $\delta$), with less dominant values sometimes (somewhat surprisingly) leading to even more pronounced separation of the side-bands than observed, for example, in figures 3(*a*) and 3(*b*). Based on our experience, however, the series presented in this subsection provides a good indication as to how the unstable class Ia evolution (using near dominant perturbations) varies with incident steepness.

### 4.3. *Simulation of class Ib short-crested wave instabilities*

Whenthe angle $\theta$ is neither too large nor too small (roughly around 55°), Ioualalen & Kharif (1994) found that the dominant lowest-order short-crested wave instability is of so-called class Ib. This type of instability has been reportedly observed in the physical experiments of Kimmoun *et al.* (1999*a*). Examples of class Ib instability regions can be found in figures 8 and 9 of Ioualalen & Kharif (1994). However, of the specific short-crested wave examples considered, only in their figure 9(*b*), with $ak = 0.20$ and $\theta = 60°$, is this type of instability dominant. We will therefore use this single case to determine the input parameters for an example simulation of a class Ib instability. From their figure 9(*b*), the dominant class Ib instability corresponds roughly to $q = 0.20$, with $p = q \tan\theta = 0.173$. The parameters used for this simulation are again summarized in tables 2 and 3.

For the simulation of the class Ib instability, the perturbation wavenumber components for the upper side-band (subscript $a$) are again as defined in (4.9), with those of the lower side-band now changed to

$$(k_{bx}, k_{by}) = (\sin\theta - p, \cos\theta - q)k. \tag{4.13}$$

The corresponding perturbation frequencies are again as defined in (3.5), with $\delta$ as given in table 2. Hence, the perturbations will now excite the two resonant quartet interactions

$$2\boldsymbol{k}_{01} = \boldsymbol{k}_{a1} + \boldsymbol{k}_{b1}, \qquad 2\boldsymbol{k}_{02} = \boldsymbol{k}_{a2} + \boldsymbol{k}_{b2}, \tag{4.14}$$

both in conjunction with (3.7). Unlike the class Ia instability, the two primary short-crested wave components $\boldsymbol{k}_{01}, \boldsymbol{k}_{02}$ are now involved in separate resonant interactions, both analogous in form to the familiar quartet resonance for a classical class I plane wave instability (3.8).

Note that dominant class Ib short-crested wave instabilities have $q > 0$, and hence generally require the resolution of multiple transverse wavelengths for their numerical simulation. To ease the computational burden, the spatial resolution has therefore been reduced slightly for the following simulation, as indicated in table 3. Additionally,

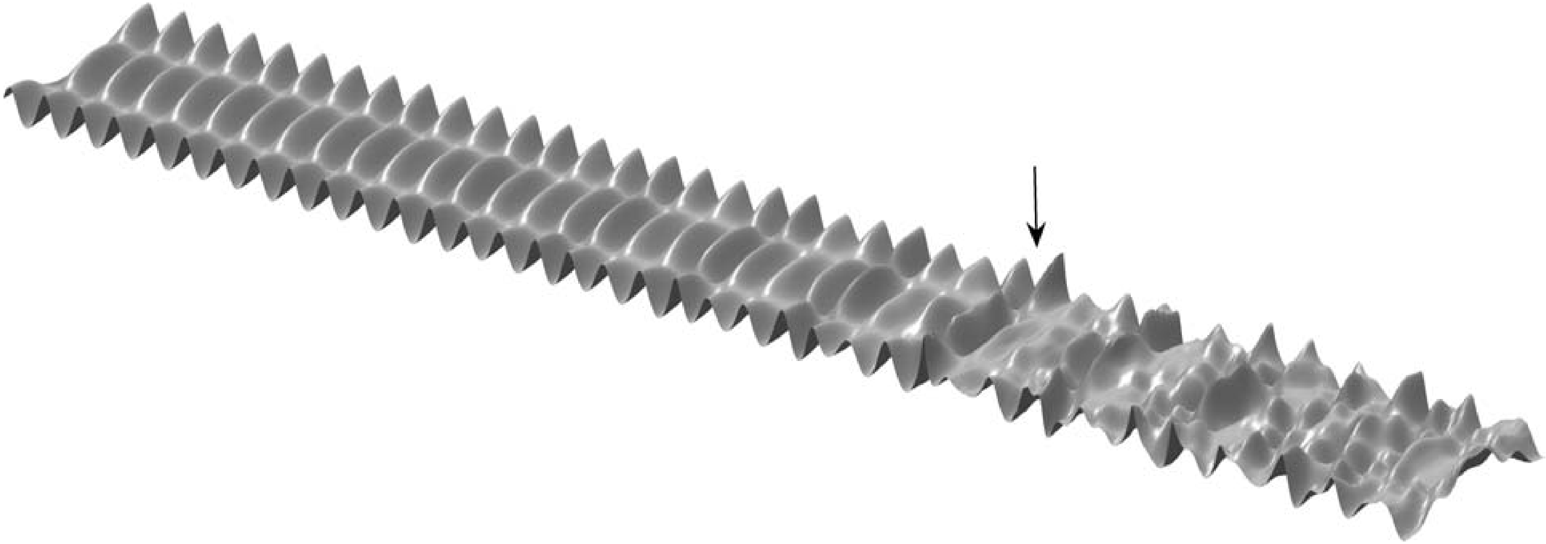

Figure 8. Computed free surface from the simulation of class Ia short-crested wave instability with $ak = 0.20$ and $\theta = 80°$, covering the range $0 \leqslant x \leqslant 40L_x$. The arrow marks the estimated location of incipient wave breaking. The vertical scale is exaggerated 15 times.

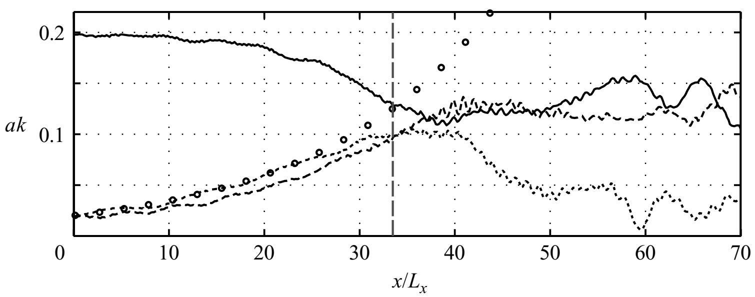

FIGURE 9. Computed evolution of the primary frequency (full line) and lower/upper side-bands (long/short dashed lines) from the simulation of class Ib short-crested wave instability with $ak = 0.20$, $\theta = 60°$ and $\epsilon = 0.10$. The circles indicate the theoretical growth as in figure 3, here with $\mathrm{Im}\{\sigma\} = 0.0044$. The dashed vertical line indicates the estimated breaking location.

the relative perturbation strength is increased to $\epsilon = 0.10$, to promote a faster growth of the unstable side-bands.

The evolution of the primary wave $\omega_0$ and the upper/lower side-bands $\omega_a/\omega_b$ for this case is shown in figure 9. The perturbations are again seen to follow closely the theoretical growth (again indicated by $\circ$) during the initial growth phase, with the upper side-band now maintaining an amplitude slightly larger than the lower. At roughly the estimated breaking location, empirically determined as before, the growth of the upper side-band ceases, maintaining a nearly constant amplitude for roughly $10L_x$, before ultimately shrinking back down to secondary importance. The lower side-band and the primary frequency maintain roughly equivalent amplitudes after the initial downshift, seemingly competing for dominance. We again stress, however, that the computed results beyond the onset of breaking should only be taken as qualitative.

The computed free surface, covering the region $0 \leqslant x \leqslant 50L_x$ for the class Ib short-crested wave simulation is shown in figure 10. Within this region, the initially (nearly) regular short-crested wave pattern first develops into one that is highly modulated. Unlike the earlier class Ia instabilities considered, however, each of the primary short-crested wave components is here independently modulated, leading to striking 'X'-shaped surface patterns. This is consistent with expectations from the resonant conditions (4.14). Beyond the estimated onset of breaking (indicated by the arrow) the free surface becomes more irregular, somewhat resembling that from the end of figure 8.

It is clearly of interest to consider additional class Ib short-crested wave instabilities, and perhaps to continue the present simulation on a longer domain. Because of the large computational demands, however, this is left for future study.

## 5. Discussion

Throughout this paper, the onset of wave breaking has been estimated using an empirical threshold for the forward surface slope, as discussed in § 3. In all cases where breaking has been detected (see again figures 1*c*, 1*d*, 3*c*, 3*d*, and 9), this estimation has coincided with a distinct qualitative break in the harmonic evolution, giving some confidence as to its physical relevance. This simple empirical threshold should not be regarded as universal, however, as the onset of wave breaking is inherently complicated. As an additional check, we will now re-visit our various results within the

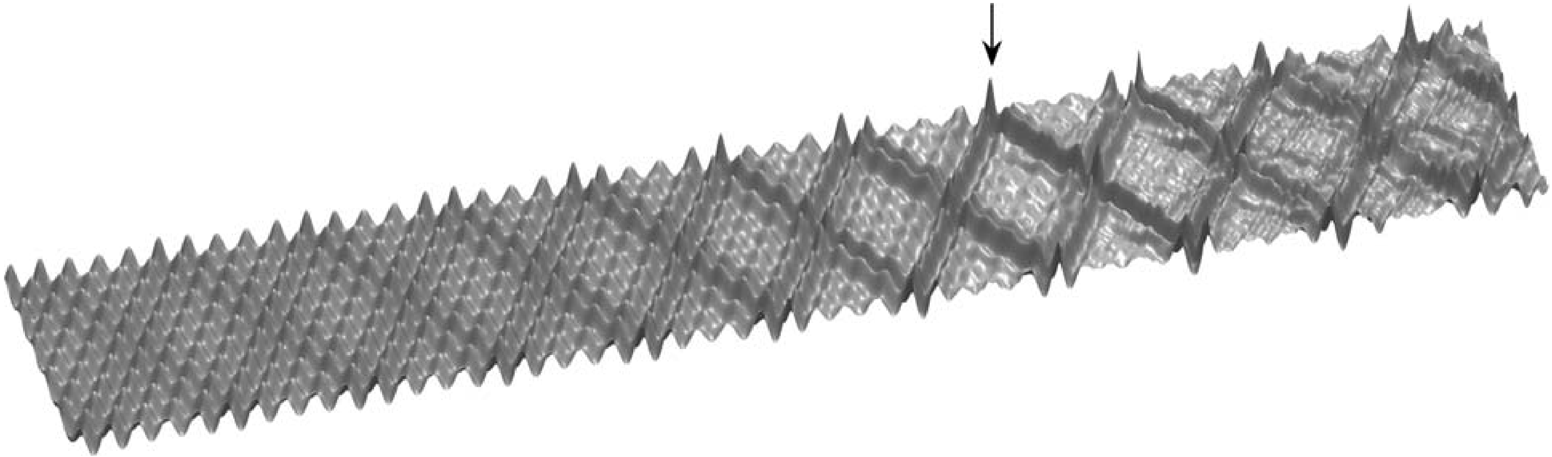

Figure 10. Computed free surface from the simulation of class Ib short-crested wave instability with $\epsilon = 0.10$, $ak = 0.20$ and $\theta = 60°$. The plot covers the region $0 \leqslant x \leqslant 50L_x$. The arrow marks the estimated location of incipient wave breaking. The vertical scale is exaggerated 20 times.

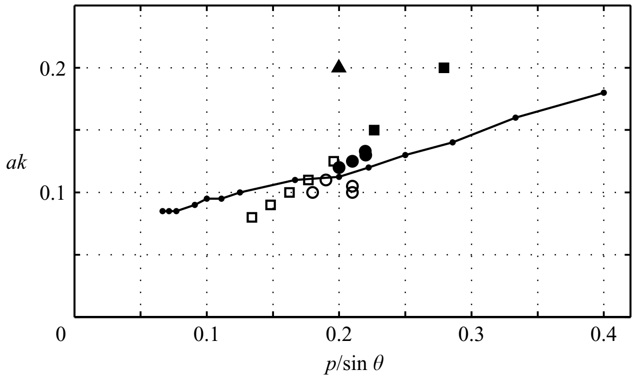

FIGURE 11. Comparison of the approximate threshold breaking incident wave steepness for class I plane wave instabilities (full line with dots, adapted from Banner & Tian 1998; Henderson *et al.* 1999) with parameters used in class I plane wave ($\theta = 90°$) simulations (circles, including results of Madsen *et al.* 2002), class Ia short-crested wave simulations with $\theta = 80°$ (squares), and the class Ib short-crested wave simulation with $\theta = 60°$ (triangle). An open/filled marker indicates a case believed to be non-breaking/breaking. Note that some class Ia cases not specifically discussed in § 4.2 are included here for completeness.

context of the class I plane wave (incident steepness) breaking thresholds of Banner & Tian (1998) and Henderson *et al.* (1999), which were used earlier in § 3. Such a comparison is, of course, only strictly valid for the plane wave cases. However, as the class Ia short-crested cases considered herein are near the plane wave limit (with $\theta = 80°$), such a comparison seems reasonable, at least as a preliminary indication. As short-crested wave instabilities for a given steepness are weaker than their plane wave counterparts (Ioualalen & Kharif 1994), there is reason to expect that the threshold breaking steepnesses for short-crested wave instabilities would be larger than for class I plane wave instabilities. This expectation is supported by table 1, which shows that the computed maximum surface slopes for a given wave steepness are generally less for the short-crested wave simulations than for the corresponding class I simulations. Moreover, Roberts (1983) found that steady short-crested waves can achieve steepnesses up to 60 % larger than plane waves, though (from his figure 4) the differences are not so pronounced, for example, with $\theta = 80°$. In any case, for the above mentioned reasons, we expect that the class I plane wave threshold steepnesses are probably conservative for short-crested wave instabilities, though this remains to be formally demonstrated.

A comparison of the parameters used in our various simulations with these earlier results is provided in figure 11. Here, the full line connects values for the lowest incident wave steepness leading to class I breaking from figure 1 of Henderson *et al.* (1999), substituting the previously mentioned value $ak = 0.1125$ from Banner & Tian (1998) (their figure 2) at $p = 0.2$ (rather than $ak = 0.12$ from Henderson *et al.* 1999). Note that the $x$-axis of figure 11 (simplifying to the variable $p$ with $\theta = 90°$) is the inverse of their $x$-axes (depicting the number of waves in one modulation). Results are shown for our computed class I plane wave cases (circles, including the results of Madsen *et al.* 2002), the class Ia short-crested wave cases (squares), as well as for the lone class Ib case (triangle, not discussed further). As was established in § 3, the computed class I results are consistent with the previously established thresholds, with all non-breaking (recurrent) cases lying below the full line, and with all breaking (asymmetric) cases above the full line.

The class Ia short-crested wave cases considered herein are also, for the most part, consistent with the class I thresholds. The lone exception is the case with $ak = 0.125$, which lies above the full line in figure 11, but does not exceed our empirical breaking threshold slope 0.61 (see table 1). Nor is there any distinct break in the harmonic and mean frequency evolutions depicted in figures 3(*b*) and 6 for this case. This apparent discrepancy is therefore not of great concern, as there is again reason to expect that the class I threshold line is conservative (i.e. too low) with respect to breaking for short-crested wave instabilities. What is perhaps the most important observation from this comparison, is that the class Ia case, e.g. with $ak = 0.10$, is well below even the (presumably conservative) class I threshold line. Hence, this comparison adds credence to our earlier conclusion, that the observed asymmetric evolution within short-crested wave instabilities is indeed part of the conservative (non-breaking) evolution. Note again that we have found similar behaviour for class Ia cases with $ak \leqslant 0.10$, which are also plotted in figure 11 for completeness.

These findings are, in many ways, qualitatively similar to those of Trulsen & Dysthe (1997), who found that a permanent downshift in the peak frequency could occur without dissipation within the context of three-dimensional class I plane wave instabilities. While none of our non-breaking simulations lead to a permanent downshift of the peak frequency, they do demonstrate a clear tendency for a permanent energy transfer to the lower (three-dimensional) side-band, which is the basic mechanism of their observed downshift. Moreover, as previously mentioned, Trulsen & Dysthe (1997) found that, even when the peak frequency was downshifted, the mean frequency tended to be slightly upshifted, consistent with our non-breaking class Ia results (e.g. with $ak = 0.125$) presented in figure 6. Alternatively, the steepest cases considered here (where dissipation from the smoothing filter is believed to have prevented wave breaking) generally lead to a permanent downshift in both the peak and mean frequencies (see again figures 3*c*, 3*d*, 5*f*, 5*h*, and 6). Hence, these simulations additionally support the conclusion of Trulsen & Dysthe (1997), that the full explanation of the frequency downshift phenomenon probably involves combined effects from the nonlinear three-dimensional evolution and dissipative wave breaking.

## 6. Conclusions

This work provides, to our knowledge, the first numerical simulations involving the instability of doubly periodic progressive short-crested waves. The simulations use a numerical finite-difference model based on the fully nonlinear high-order Boussinesq-type formulation of Madsen *et al.* (2002), as described by Fuhrman & Bingham (2004). As incident waves, the third-order short-crested solution of Hsu *et al.* (1979) has been used, perturbed to excite the desired instability based on the analysis of Ioualalen & Kharif (1994). These simulations have been limited to the study of lowest-order short-crested wave instabilities (involving quartet resonant interactions), of so-called class Ia and Ib.

Before considering short-crested wave simulations, however, the numerical model has first been used to simulate a series of two-dimensional class I instabilities, with steepness both above and below previously established breaking threshold (incident wave) steepnesses from Banner & Tian (1998) and Henderson *et al.* (1999). It is shown that below the threshold, the model correctly predicts the well-known classical (nearly symmetric) recurrence cycle, whereas above this threshold, the evolution leads to an asymmetric evolution, characterized by a permanent transfer of energy to the lower side-band, with a smoothing filter apparently serving as the dissipative mechanism promoting this behaviour for sufficiently steep waves. This series of simulations convincingly demonstrates the ability of the model to predict accurately the correct qualitative behaviour in these well-known (and closely related) physical circumstances. Additionally, these simulations have been used to formulate an empirical breaking threshold surface slope, used throughout this work to estimate the location of incipient breaking.

This numerical study has primarily focused on the simulation of class Ia instabilities, which are known to be dominant when short-crested waves are near their standing ($\theta = 0^\circ$) and plane wave ($\theta = 90^\circ$) limits. This type of instability involves simultaneous resonant interactions of both short-crested wave components with those from two separate short-crested perturbation waves. These simulations have considered cases near the plane wave limit (with $\theta = 80^\circ$), covering the range of incident wave steepness $0.10 \leqslant ak \leqslant 0.20$. A close match of the computed and theoretical unstable growth rates is obtained near the inception, further validating the model. The long-term evolution of these short-crested wave instabilities is shown to be qualitatively different from the well-known evolution of classical class I plane wave instabilities. Rather than following a nearly symmetric recurrence cycle, there is a permanent transfer of energy to the lower side-band after the initial growth phase (of a quasi-recurrence cycle), even in weakly nonlinear simulations presumably well below breaking. This is also accompanied by an additional transfer of energy to more distant upper side-bands, which in turn tends to cause an upshift in the mean frequency.

As the steepness is further increased ($ak \geqslant 0.15$), there is a permanent downshift in both the peak and mean frequencies (driven in part by dissipation from the filter), with the lower side-band rising to a permanent strength near that of the primary incident wave, effectively breaking the recurrence cycle. Based on our empirical surface slope threshold, however, these cases would lead to physical breaking, and have therefore only been qualitatively modelled beyond this location. In these cases the downshift is accompanied by the chaotic (disorderly) evolution of the primary frequency and upper side-band.

Computed free surfaces have also been shown for class Ia cases having initial steepness $ak = 0.10$ and 0.20, corresponding, respectively, to weakly and highly nonlinear cases. The weakly nonlinear case (following a quasi-recurrent evolution) is shown to lead to the formation of steep three-dimensional pulses on the free surface, in some ways analogous to the classical weakly nonlinear two-dimensional (class I) evolution. The computed free surface from the steeper simulation follows a similar evolution to the estimated breaking location, followed by the rapid disintegration of the initially regular short-crested wavefield into a rather irregular free surface.

A single case of class Ib instability has also been considered; this type of instability is known to dominate when the short-crested waves are more three-dimensional, with $\theta \approx 55^\circ$. For this type of instability, the two components of the incident short-crested wave are involved in separate resonant interactions. As the transverse perturbation wavenumbers for dominant class Ib instabilities do not match those of the primary short-crested wave, the numerical simulation of this phenomenon is generally more computationally demanding than for class Ia, requiring the resolution of multiple transverse primary wavelengths. Hence, the current investigation has been limited to the lone case with $ak = 0.20$ and $\theta = 60^\circ$, again inspired by the analysis of Ioualalen & Kharif (1994). The computed growth rate again closely matches the theory up to the estimated location of incipient breaking. Beyond this point, the evolution is qualitatively similar to the steeper class Ia cases, with the primary frequency and lower side-band in this case seemingly competing for dominance. The computed free

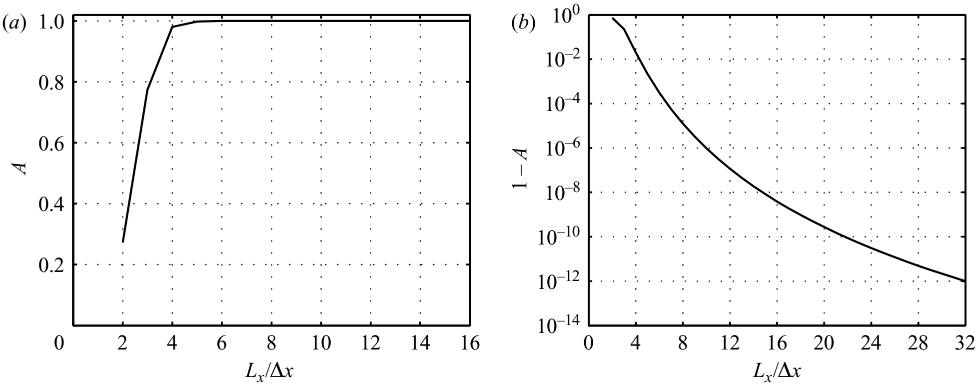

FIGURE 12. Amplification portraits from a Fourier analysis of the tenth-order, 109-point Savitzky–Golay smoothing filter used in the numerical simulations.

surface initially leads to striking ‘X’-shaped patterns (as both primary short-crested wave components are individually modulated), before ultimately becoming irregular in its appearance following the initial downshift.

The simulations considered in this work represent the simplest physical scenarios for the study of three-dimensional instabilities of genuinely three-dimensional progressive waves. These simulations are therefore of fundamental importance in understanding three-dimensional wave spectrum development. The results add to mounting evidence that the conservative (non-breaking) evolution of three-dimensional spectra can be qualitatively different than predicted by classical two-dimensional descriptions.

We wish to thank the Danish Technical Research Council (STVF grant 9801635) for financial support, and the Danish Center for Scientific Computing for providing super-computing resources. Their support is greatly appreciated.

## Appendix. Fourier analysis of the Savitzky–Golay smoothing filter

In this Appendix we quantify the dissipative effects from the tenth-order (109-point, octagon-shaped) Savitzky & Golay (1964) type smoothing filter employed throughout this work. To simplify the analysis, we consider a single horizontal dimension, which corresponds to summing the columns (or rows) of the two-dimensional filter. This leads to the one-dimensional 13-point filter

$$[-0.000311 \quad 0.00373 \quad -0.0205 \quad 0.0684 \quad -0.154 \quad 0.246 \quad 0.713 \\ 0.246 \quad -0.154 \quad 0.0684 \quad -0.0205 \quad 0.00373 \quad -0.000311],$$

where the first three significant digits are shown for each coefficient. We consider a single application of the filter on a sinusoidal mode having wavelength $L_x$. Thus, the quantity $L_x/\Delta x$ defines the spatial resolution in terms of the number of grid points per wavelength. A standard Fourier analysis leads to the amplification portraits depicted in figure 12, where $A$ is the amplification factor for a given resolution. Thus, $A < 1$ implies dissipation of a given mode. Clearly, from figure 12(*a*), significant dissipation is limited to high wavenumber modes, discretized with roughly $L_x/\Delta x \leqslant 4$. In most of the simulations considered herein, this corresponds physically, for example, to bound eighth (and higher) harmonics, provided that the primary wavelength is discretized with 32 grid points. As the resolution is increased, the amplification factor rapidly approaches unity. For example, as seen in figure 12(*b*), any dissipation of such a primary wavelength discretized with 32 grid points is negligible, with $(1 - A) = 10^{-12}$.

## REFERENCES

Badulin, S. I., Shrira, V. I., Kharif, C. & Ioualalen, M. 1995 On two approaches to the problem of instability of short-crested water waves. *J. Fluid Mech.* **303**, 297–326.

Banner, M. L. & Tian, X. 1998 On the determination of the onset of breaking for modulating surface gravity water waves. *J. Fluid Mech.* **367**, 107–137.

Benjamin, T. B. & Feir, J. E. 1967 The disintegration of wavetrains on deep water. Part 1. Theory. *J. Fluid Mech.* **27**, 417–430.

Bryant, P. J. 1985 Doubly periodic progressive permanent waves in deep water. *J. Fluid Mech.* **161**, 27–42.

Cash, J. R. & Karp, A. H. 1990 A variable order Runge–Kutta method for initial value problems with rapidly varying right-hand sides. *ACM Trans. Math. Software* **16**, 201–222.

Dold, J. W. & Peregrine, D. H. 1986 Water-wave modulation. In *Proc. 20th Intl Conf. Coastal Engineering* (ed. B. L. Edge), vol. 1, pp. 163–175. Taipei.

Dysthe, K. B., Trulsen, K., Krogstad, H. E. & Socquet Juglard, H. 2003 Evolution of a narrow-band spectrum of random surface gravity waves. *J. Fluid Mech.* **478**, 1–10.

Fenton, J. D. 1988 The numerical solution of steady water wave problems. *Comput. Geosci.* **14**, 357–368.

Fructus, D., Kharif, C., Francius, M., Kristiansen, O., Clamond, D. & Grue, J. 2005 Dynamics of crescent water wave patterns. *J. Fluid Mech.* **537**, 155–186.

Fuhrman, D. R. & Bingham, H. B. 2004 Numerical solutions of fully non-linear and highly dispersive Boussinesq equations in two horizontal dimensions. *Intl J. Numer. Meth. Fluids* **44**, 231–255.

Fuhrman, D. R. & Madsen, P. A. 2005 Potential dominance of oscillating crescent waves in finite width tanks. *Phys. Fluids* **17**, 038102/1–4.

Fuhrman, D. R. & Madsen, P. A. 2006 Short-crested waves in deep water: a numerical investigation of recent laboratory experiments. *J. Fluid Mech.* **559**, 391–411.

Fuhrman, D. R., Madsen, P. A. & Bingham, H. B. 2004 A numerical study of crescent waves. *J. Fluid Mech.* **513**, 309–341.

Hammack, J., Henderson, D. M. & Segur, H. 2005 Progressive waves with persistent two-dimensional surface patterns in deep water. *J. Fluid Mech.* **532**, 1–52.

Hara, T. & Mei, C. C. 1991 Frequency downshift in narrowbanded surface waves under the influence of wind. *J. Fluid Mech.* **230**, 429–477.

Henderson, D. M., Patterson, M. S. & Segur, H. 2006 On the laboratory generation of two-dimensional, progressive, surface waves of nearly permanent form on deep water. *J. Fluid Mech.* **559**, 413–427.

Henderson, K. L., Peregrine, D. H. & Dold, J. W. 1999 Unsteady water wave modulations: fully nonlinear solutions and comparison with the nonlinear Schrödinger equation. *Wave Motion* **29**, 341–361.

Hsu, J. R., Tsuchiya, Y. & Silvester, R. 1979 Third-order approximation to short-crested waves. *J. Fluid Mech.* **90**, 179–196.

Ioualalen, M. & Kharif, C. 1994 On the subharmonic instability of steady three-dimensional deep water waves. *J. Fluid Mech.* **262**, 265–291.

Ioualalen, M., Roberts, A. J. & Kharif, C. 1996 On the observability of finite-depth short-crested water waves. *J. Fluid Mech.* **322**, 1–19.

Ioualalen, M., Kharif, C. & Roberts, A. J. 1999 Stability regimes of finite depth short-crested water waves. *J. Phys. Oceanogr.* **29**, 2318–2331.

Kimmoun, O., Branger, H. & Kharif, C. 1999*a* On short-crested waves: experimental and analytical investigations. *Eur. J. Mech. B/Fluids* **18**, 889–930.

Kimmoun, O., Ioualalen, M. & Kharif, C. 1999*b* Instabilities of steep short-crested surface waves in deep water. *Phys. Fluids* **11**, 1679–1681.

Lake, B. M., Yuen, H. C., Rungaldier, H. & Ferguson, W. E. 1977 Nonlinear deep-water waves: theory and experiments. Part 2. Evolution of a continuous wavetrain. *J. Fluid Mech.* **83**, 49–74.

Lo, E. & Mei, C. C. 1985 A numerical study of water-wave modulation based on a higher-order nonlinear Schrödinger equation. *J. Fluid Mech.* **150**, 395–416.

Lo, E. Y. & Mei, C. C. 1987 Slow evolution of nonlinear deep water waves in two horizontal directions: a numerical study. *Wave Motion* **9**, 245–259.

McLean, J. W. 1982*a* Instabilities of finite-amplitude gravity waves on water of finite depth. *J. Fluid Mech.* **114**, 331–341.

McLean, J. W. 1982*b* Instabilities of finite-amplitude water waves. *J. Fluid Mech.* **114**, 315–330.

Madsen, P. A., Bingham, H. B. & Liu, H. 2002 A new Boussinesq method for fully nonlinear waves from shallow to deep water. *J. Fluid Mech.* **462**, 1–30.

Madsen, P. A., Bingham, H. B. & Schäffer, H. A. 2003 Boussinesq-type formulations for fully nonlinear and extremely dispersive water waves: derivation and analysis. *Proc. R. Soc. Lond.* A **459**, 1075–1104.

Melville, W. K. 1982 The instability and breaking of deep-water waves. *J. Fluid Mech.* **115**, 165–185.

Onorato, M., Osborne, A. R., Serio, M., Resio, D., Pushkarev, A., Zakharov, V. E. & Brandini, C. 2002 Freely decaying weak turbulence for sea surface gravity waves. *Phys. Rev. Lett.* **89**, 144501.1–4.

Roberts, A. J. 1983 Highly nonlinear short-crested water waves. *J. Fluid Mech.* **135**, 301–321.

Roberts, A. J. & Peregrine, D. H. 1983 Notes on long-crested water waves. *J. Fluid Mech.* **135**, 323–335.

Saad, Y. & Schultz, M. H. 1986 GMRES: a generalized minimal residual algorithm for solving nonsymmetric linear systems. *SIAM J. Sci. Stat. Comput.* **7**, 856–869.

Savitzky, A. & Golay, M. J. E. 1964 Smoothing and differentiation of data by simplified least squares procedures. *Anal. Chem.* **36**, 1627–1639.

Shemer, L. & Chamesse, M. 1999 Experiments on nonlinear gravity–capillary waves. *J. Fluid Mech.* **380**, 205–232.

Shrira, V. I., Badulin, S. I. & Kharif, C. 1996 A model of water wave 'horse-shoe' patterns. *J. Fluid Mech.* **318**, 375–404.

Skandrani, C., Kharif, C. & Poitevin, J. 1996 Nonlinear evolution of water surface waves: the frequency downshift phenomenon. *Contemp. Maths* **200**, 157–171.

Sørensen, O. R., Madsen, P. A. & Schäffer, H. A. 1998 Nearshore wave dynamics simulated by Boussinesq type models. In *Proc. 21st Intl Conf. Coastal Engineering* (ed. B. L. Edge), vol. 1, pp. 272–285. Copenhagen.

Stiassnie, M. & Kroszynski, U. I. 1982 Long-time evolution of an unstable water-wavetrain. *J. Fluid Mech.* **116**, 207–225.

Stiassnie, M. & Shemer, L. 1987 Energy computations for evolution of class I and II instabilities of Stokes waves. *J. Fluid Mech.* **174**, 299–312.

Su, M. Y., Bergin, M., Marler, P. & Myrick, R. 1982 Experiments on nonlinear instabilities and evolution of steep gravity-wavetrains. *J. Fluid Mech.* **124**, 45–72.

Trulsen, K. & Dysthe, K. B. 1990 Frequency down-shift through self modulation and breaking. In *Water Wave Kinematics* (ed. A. Tørum & O. T. Gudmestad), pp. 561–572. Kluwer.

Trulsen, K. & Dysthe, K. B. 1996 A modified nonlinear Schrödinger equation for broader bandwidth gravity waves on deep water. *Wave Motion* **24**, 281–289.

Trulsen, K. & Dysthe, K. B. 1997 Frequency downshift in three-dimensional wavetrains in a deep basin. *J. Fluid Mech.* **352**, 359–373.

Trulsen, K., Stansberg, C. T. & Velarde, M. G. 1999 Laboratory evidence of three-dimensional frequency downshift of waves in a long tank. *Phys. Fluids* **11**, 235–237.

Tulin, M. P. & Waseda, T. 1999 Laboratory observations of wave group evolution, including breaking effects. *J. Fluid Mech.* **378**, 197–232.

Xue, M., Xü, H., Liu, Y. & Yue, D. K. P. 2001 Computations of fully nonlinear three-dimensional wave-wave and wave-body interactions. Part 1. Dynamics of steep three-dimensional waves. *J. Fluid Mech.* **438**, 11–39.